Constraints on the strength of first-order phase transition in the low density region

Bikai Gao[1]

[1]*Research Center for Nuclear Physics (RCNP), Osaka University, Osaka 567-0047, Japan*

ABSTRACT

We systematically studied the first-order phase transitions in the low-density region of neutron star matter using a unified framework combining the parity doublet model for hadronic matter, an NJL-type quark model for high-density quark matter, and a model-independent intermediate region treatment. By confronting with recent neutron star observation constraints, we find it possible to have the early phase transitions (PT) at low densities ($n_B \leq 2n_0$) in a way consistent with existing neutron star observations. We also establish the upper limits of the PT strength for each chiral invariant mass in parity doublet model. We find that larger chiral invariant mass lead to smaller allowed phase transition strengths, providing new insights and clue into nucleon mass origin. This connection between the microscopic structure of nucleons and macroscopic neutron star properties shows how astrophysical observations can constrain fundamental QCD mechanisms underlying hadron mass generation.

1. INTRODUCTION

The equation of state (EOS) of dense nuclear matter is crucial for understanding neutron star (NS) structure and evolution. Of particular significance is the potential existence of phase transitions (PT) within NS interiors, where hadronic matter may transit to exotic states such as quark matter through crossover or first-order PT. First-order PTs are characterized by discontinuous jumps in energy density and baryon number density while maintaining continuity in pressure and chemical potential. Unlike continuous crossovers (Baym et al. (2018, 2019); Kojo et al. (2022)), the discontinuities introduced by first-order PTs can significantly alter NS observation properties, producing distinctive signatures in both electromagnetic and gravitational wave observations Lenzi & Lugones (2012); Benic et al. (2015); Christian et al. (2024); Gao et al. (2024b). In cases of sufficiently strong first-order PTs, the mass-radius (M-R) relationship may even develop disconnected branches, potentially leading to "twin stars"— NSs with similar masses but significantly different radii Benic et al. (2015); Alford & Sedrakian (2017); Most et al. (2018).

bikai@rcnp.osaka-u.ac.jp

While first-order PTs can occur at various densities within NSs, those occurring in the low-density region ($n_B \leq 2n_0$) are of particular significance. First, this density regime is accessible to heavy-ion collision experiments, providing unique opportunities for terrestrial validation of theoretical predictions (Busza et al. (2018)). Second, the EOS at 1-2n_0 strongly influences NS radii, making this region critical for interpreting NS observations. Furthermore, gravitational waves from NS mergers can probe this density range, with first-order PTs producing potentially detectable signatures in the waveforms of next-generation detectors, offering a unique window into fundamental physics in this finite density region (Fujimoto et al. (2023); Huang et al. (2022); Guo et al. (2025)).

Despite extensive theoretical studies exploring about the PTs, systematic constraints on the strength and character of first-order PTs specifically in the low-density regime remain relatively unexplored. The strength of such transitions, characterized by the magnitude of the density discontinuity δn_B and energy density jump $\delta\varepsilon$, has yet to be constrained using current astrophysical observations within a physically consistent theoretical framework.

In this work, we address this gap by presenting a systematic analysis constraining the allowable strength of first-order PTs in the low-density region of NS matter. We employ a physically motivated framework combin-

ing three key components: (1) the parity doublet model (PDM) (Detar & Kunihiro (1989); Jido et al. (2001); Minamikawa et al. (2021); Zschiesche et al. (2007); Dexheimer et al. (2008); Sasaki & Mishustin (2010); Motohiro et al. (2015); Marczenko et al. (2020, 2022); Kong et al. (2023); Gao et al. (2024a,b)) for the hadronic phase, capturing essential features of chiral symmetry in nuclear matter; (2) an NJL-type quark model for high-density matter (Hatsuda & Kunihiro (1994); Baym et al. (2018, 2019); Kojo et al. (2022); Gao et al. (2022); Yuan & Li (2024); Gao et al. (2024a,b); Gholami et al. (2024)), incorporating both vector repulsion and color superconductivity; and (3) a model-independent approach based on thermodynamic principles for the intermediate density region (Komoltsev & Kurkela (2022)).

This unified approach enables us to systematically explore the parameter space of possible PT while maintaining consistency with both nuclear physics constraints and astronomical observations. By combining theoretical modeling with observational data from NICER and gravitational wave detections, we establish bounds on the strength of potential first-order PTs in the low-density region.

The paper is structured as follows: In the remainder of Section 1, we describe our theoretical framework, including the hadronic regime modeled through the PDM, the quark matter regime described by the NJL model, and our approach to the intermediate density region. Section 2 presents our numerical results, including our methodology for constraining PT strengths and their implications for NS observables. In Section 3, we summarize our findings and discuss their broader implications for nuclear physics and NS astrophysics.

1.1. *The Hadronic regime*

For the low-density hadronic region ($n_B \leq n_L$), we employ the PDM following Gao et al. (2022); Minamikawa et al. (2023), where n_L denotes the upper density limit for which the PDM description is applied. The parameters of our PDM are determined by fitting to physical inputs in vacuum (Pion decay constant $f_\pi = 93$ MeV and hadron masses) and properties of normal nuclear matter (Saturation density $n_0 = 0.16$ fm^{-3}, binding energy $B_0 = 16$ MeV, incompressibility $K_0 = 240$ MeV, and symmetry energy $S_0 = 31$ MeV). The model also incorporates vector meson ω-ρ mixing interaction, which significantly impacts the slope parameter L_0 of the symmetry energy.

In contrast to traditional models such as the linear σ model, which assume that nucleon mass arises entirely from spontaneous chiral symmetry breaking with the σ field serving as the order parameter, the PDM in-

troduces a fundamentally different perspective. Within the PDM framework, nucleons possess a chiral invariant mass m_0 that does not depend on the σ field and remains insensitive to environment. This approach provides new insights into the nature of nucleon mass by decomposing it as $m_N = m_0 + m_\sigma$, where m_0 represents the chiral invariant component and m_σ represents the contribution from chiral symmetry breaking (Weinberg (1969)). We systematically explore the parameter space by varying the parameter chiral invariant mass m_0 with the slope parameter L_0 fixed to be 57.7 MeV consistent with Ref. Li et al. (2021). It turns out that PDM EOS with larger values of m_0 lead to softer EOSs in the hadronic phase as shown in Fig. 1. The resulting EOS can be compared with the data-driven EOSs inferred from deep learning (edged by dotted red curves Fujimoto et al. (2021)) and Bayesian (edged by blue dotted Raaijmakers et al. (2021) and black dotted curves Ozel et al. (2016); Bogdanov et al. (2016)) analyses. For $m_0 = 500$ MeV, we find that the EOS becomes excessively stiff, falling outside the bounds of all data-driven analyses. Therefore, we restrict our investigation to the range $600 \leq m_0 \leq 900$ MeV for this study. The resulting EOS from our PDM provides the low-density anchor for our unified NS EOS, which will be connected to higher densities as described in subsequent sections.
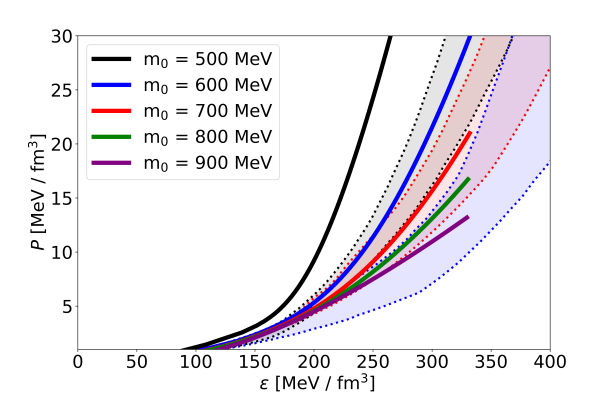

Figure 1. EOS in the PDM for different chiral invariant mass m_0 with fixed slope parameter $L_0 = 57.7$ MeV. Red band show data-driven EOSs inferred from deep learning (edged by dotted red curves Fujimoto et al. (2021)) and Bayesian (edged by blue dotted Raaijmakers et al. (2021) and black dotted curves Ozel et al. (2016); Bogdanov et al. (2016)) analyses.

1.2. *The quark matter regime*

At high densities ($n_B \gtrsim 5n_0$) where quarks become the relevant degrees of freedom, we employ the NJL-type quark model to describe the quark matter (Hatsuda & Kunihiro (1994); Baym et al. (2018, 2019); Kojo et al.

(2022); Yuan & Li (2024); Gao et al. (2024a,b); Gholami et al. (2024); Gao & Harada (2025); Yuan et al. (2025)). At such densities, the quark matter enters a strongly coupled regime with baryon chemical potential μ_B in the range ~ 1.5-2 GeV. While asymptotic freedom suggests quarks should be the fundamental degrees of freedom at these densities, the strong coupling constant α_s remains $\mathcal{O}(1)$, making perturbative QCD calculations unreliable.

The NJL model captures essential features of QCD including dynamical chiral symmetry breaking and color superconductivity, while treating gluonic degrees of freedom implicitly through effective four-fermion interactions. Our model includes quarks of three flavors (up, down, and strange) and three colors. Two key parameters govern the behavior of matter in this regime: the vector coupling g_V and the diquark coupling H. The vector coupling g_V represents the strength of repulsive vector-channel interactions between quarks while the diquark coupling H determines the strength of attractive quark-quark interactions in the color superconducting channels, leading to color superconductivity at high densities.

Following Baym et al. (2018); Kojo et al. (2022), we treat g_V and H as independent parameters in this non-perturbative regime. The allowed ranges of these parameters are constrained by fundamental physical requirements. These constraints, combined with astronomical observations like the existence of massive NSs, provide bounds on the parameter space of the model.

1.3. Intermediate density region

For the intermediate density region ($n_L \leq n_B \leq 5n_0$), we employ a model-independent approach based on fundamental physical principles (Komoltsev & Kurkela (2022)). This method requires matching conditions between the PDM at the lower boundary (P_L, n_L, μ_L) and the NJL model at the upper boundary (P_H, n_H, μ_H with $n_H = 5n_0$). The physical constraints in this region arise from two requirements: (a) Thermodynamic stability: pressure increases monotonically with chemical potential. (b) Causality condition: sound velocity $c_s^2 \leq 1$.

Thermodynamic consistency requires that pressure be a continuous function of chemical potential, yielding the integral constraint:

$$\int_{\mu_L}^{\mu_H} n_B(\mu)d\mu = P_H - P_L \tag{1}$$

These constraints define a bounded region in the pressure-energy density (P-ε) plane, with the upper boundary representing the stiffest possible EOS and the lower boundary the softest possible EOS that connect the hadronic and quark matter phases while satisfying physical requirements.

This approach offers several advantages over traditional approaches. First, it remains model-independent, relying only on fundamental physical principles; Second, it provides robust constraints without requiring detailed knowledge of microscopic physics; and also it naturally accommodates various scenarios of quark-hadron transitions without assuming their specific nature, whether smooth crossover or first-order PT.

2. NUMERICAL RESULTS

In this section, we present our analysis constraining the strength of first-order PTs in the low-density region.

2.1. Methodology

We begin by establishing a systematic procedure for connecting hadronic and quark matter EOS. For a fixed hadronic EOS in the low-density region and a fixed quark EOS in the high-density region, we determine whether these can be connected while satisfying fundamental constraints of thermodynamic stability and causality. When such a connection is possible, we obtain both upper and lower boundaries in the intermediate density region, with the upper boundary representing the stiffest physically allowable connection between the low and high-density regimes.

As illustrated in Fig. 2, we employ a hadronic EOS with $m_0 = 600$ MeV (thick grey curve) and a quark EOS with $(H, g_V)/G = (1.6, 1)$ (thick black curve). For demonstration purposes, we set the initial matching density n_L at $1.5n_0$—chosen to remain within the reliable hadronic regime while exploring our target low-density phase transition region—and determine the corresponding pressure P_L, chemical potential μ_L, as well as the high-density values P_H, $n_H = 5n_0$ (where quark degrees of freedom should become relevant), and μ_H in the NJL-type quark model. This yields the upper boundary shown by the thin skyblue curve in Fig. 2. We then model first-order PTs by introducing a density jump while preserving thermodynamic consistency. Specifically, we keep the values of P_L and μ_L unchanged while increasing the matching density as

$$n_L^{\text{new}} = n_L + \delta n_B \tag{2}$$

This approach naturally incorporates the definition of first-order PTs: pressure and baryon chemical potential are continuous, while allowing discontinuous in baryon number density and energy density.

To quantify constraints on transition strength, we increase δn_B from 0 to $1.5n_0$. The blue curve represents the case where $\delta n_B = n_0$ ($n_L^{\text{new}} = 2.5n_0$), while the green curve shows $\delta n_B = 1.5n_0$ ($n_L^{\text{new}} = 3n_0$). Following the implementation of these first-order transitions,

we recalculate the corresponding upper boundaries for each case. As δn_B increases, the resulting upper boundary becomes progressively softer. This continues until reaching a critical threshold beyond which, for sufficiently large δn_B around $2.5n_0$, the matching conditions (P_L, n_L^{new}, μ_L) cannot connect with the quark EOS without violating either thermodynamic stability or causality constraints. This effectively establishes an upper limit on the allowable strength of first-order PTs in the low-density regime.
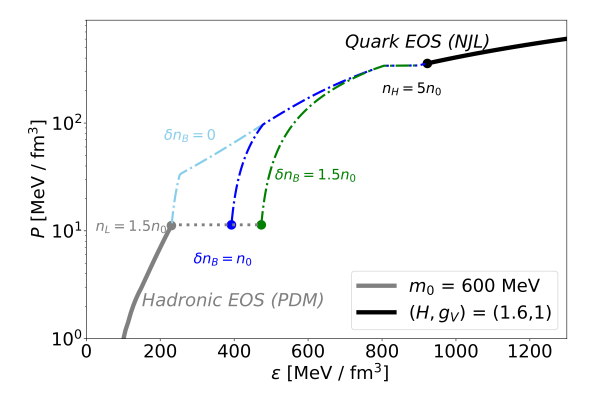

Figure 2. EOS connections between the hadronic phase described by the PDM with $m_0 = 600$ MeV (thick grey curve) and the quark phase with $(H, g_V)/G = (1.6, 1)$ (thick black curve) in the pressure versus energy density plane. The colored curves represent the upper boundaries (stiffest possible EOS) for different strengths of first-order PTs: $\delta n_B = 0$ (skyblue curve), $\delta n_B = n_0$ (blue curve), and $\delta n_B = 1.5n_0$ (green curve).

Figure 3. M-R relation for EOS connections between the hadronic phase described by the PDM with $m_0 = 600$ MeV (thick grey curve) and the quark phase with $(H, g_V)/G = (1.6, 1)$ (thick black curve). The colored curves represent the upper boundaries (stiffest possible EOS) for different strengths of first-order PTs: $\delta n_B = 0$ (skyblue curve), $\delta n_B = n_0$ (blue curve), and $\delta n_B = 1.5n_0$ (green curve).
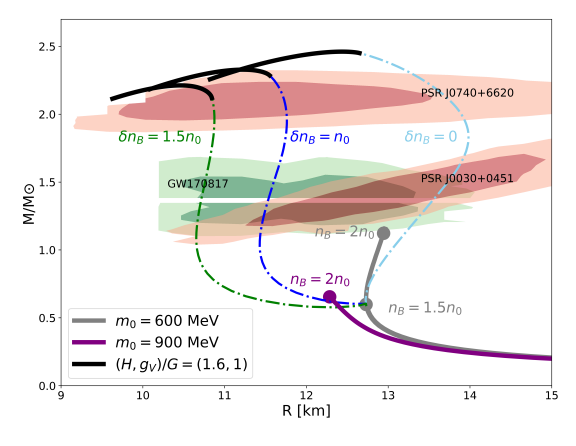
2.2. NS Properties and Observational Constraints

By solving the Tolman-Oppenheimer-Volkoff (TOV) equations, we derive the M-R relations corresponding to each upper boundary EOS with different δn_B values, as shown in Fig. 3. These theoretical M-R curves can be directly compared with recent NS observations, including NICER measurements of PSR J0030+0451 (Miller et al. 2019) ($M = 1.44^{+0.07}_{-0.07}\,M_\odot$, $R = 13.7^{+2.6}_{-1.5}$ km) and PSR J0740+6620 (Miller et al. 2021) ($M = 2.08^{+0.07}_{-0.07}\,M_\odot$, $R = 13.7^{+2.6}_{-1.5}$ km), as well as radius constraints derived from LIGO-Virgo gravitational wave observations (Abbott et al. 2017a,b, 2018).

Since we employ the upper boundary EOS representing the stiffest possible connection between hadronic phase and quark phase, if this maximally stiff EOS with a given δn_B fails to satisfy observational constraints (e.g. cannot support the 2 $M_\odot$ mass; the radius is smaller than the observation constraints), we can conclusively rule out that transition strength. This provides a robust method for constraining the allowable range of δn_B.

In Fig. 3, we present M-R curves for pure hadronic EOSs with $m_0 = 600$ MeV (thick grey curve) and $m_0 = 900$ MeV (thick purple curve). As an example, we connect the hadronic EOS with $m_0 = 600$ MeV to the quark EOS with $(H, g_V)/G = (1.6, 1)$ (thick black curve), showing results for transition strengths of $\delta n_B = 0$ (skyblue), n_0 (blue), and $1.5n_0$ (green). As expected, increasing δn_B leads to softer EOSs and smaller radii at a given mass. For $\delta n_B = 0$, while the corresponding M-R curve has a radius at $1.4M_\odot$ of 13.8 km, larger than the 1σ confidence region for GW 170817, we cannot exclude this transition strength as softer intermediate EOSs (between upper and lower bounds) could still satisfy all constraints. For $\delta n_B = n_0$, all the observations are satisfied within 1σ level, indicating that PT strength $\delta n_B = n_0$ is still allowed. However, for $\delta n_B = 1.5n_0$, the M-R curve violates the PSR J0030+0451 constraints at the 1σ level, and there do not exist even stiffer intermediate EOS. Therefore, requiring consistency with all observations at the 1σ confidence level excludes PTs with strength $\delta n_B \geq 1.5n_0$ for our selected hadronic and quark EOS parameters.

While our previous analysis in Fig. 2 and Fig. 3 fixed the quark EOS parameters for demonstration purposes, we now systematically explore the full parameter space. For a given hadronic EOS with fixed m_0 and matching density n_L, the quark phase is characterized by H and g_V parameters. We examine how the allowable parameter region changes with increasing transition strength δn_B, as illustrated in Fig. 4. In each panel of Fig. 4, cross markers indicate parameter combinations that violate thermodynamic stability requirements. The
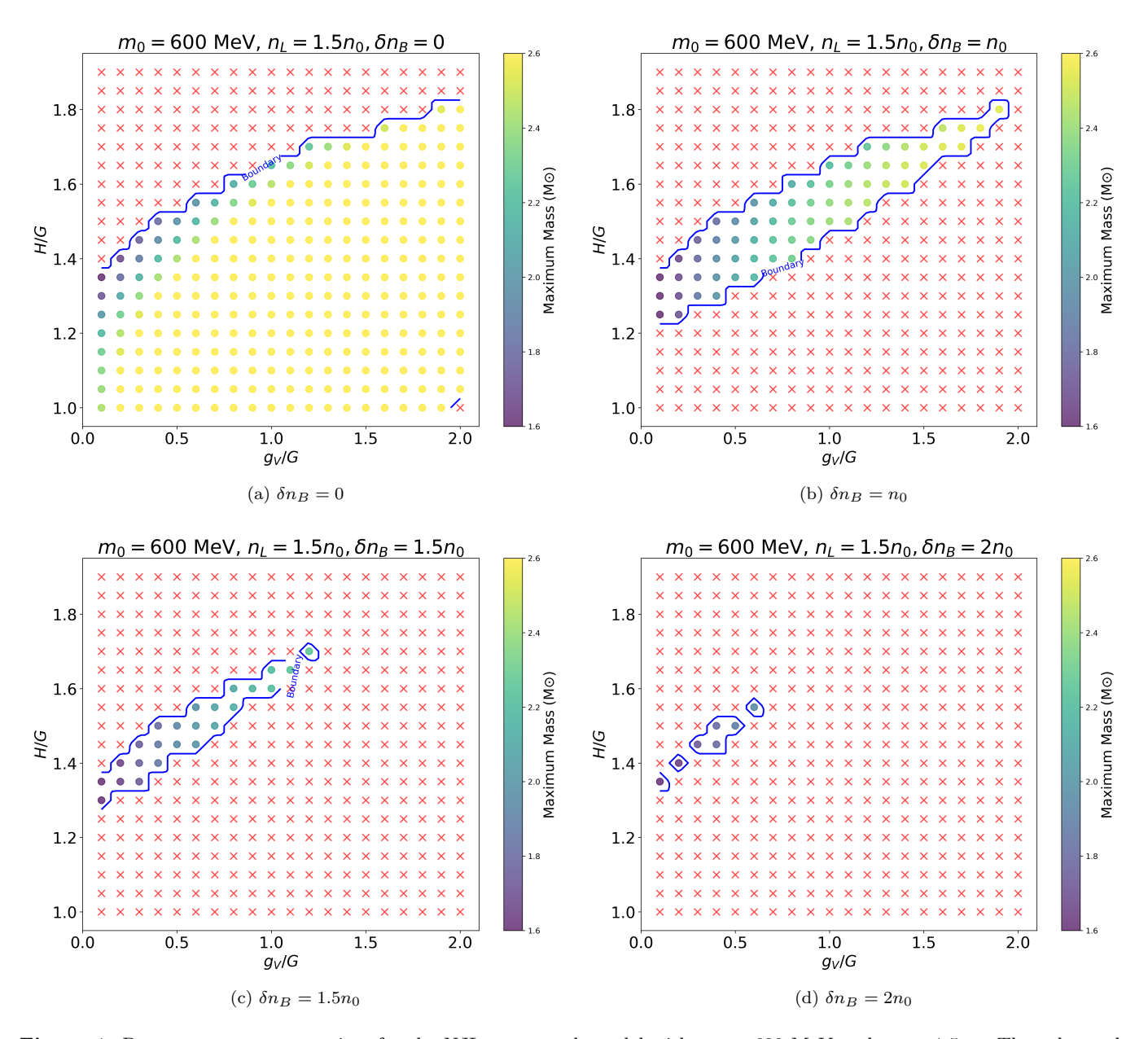
Figure 4. Parameter space constraints for the NJL-type quark model with $m_0 = 600$ MeV and $n_L = 1.5n_0$. The color scale represents the maximum NS mass achievable with each $(H, g_V)/G$ parameter combination. Cross marks indicate parameter combinations that violate thermodynamic stability requirements.

color scale represents the maximum NS mass achievable with each $(H, g_V)/G$ parameter combination. As δn_B increases, the allowed parameter region shrinks, and the corresponding maximum mass values decrease. At $\delta n_B = 2n_0$, only a small region of parameter space remains viable, and none of these remaining parameter combinations can support NSs with masses over $2M_\odot$. This excludes transitions of strength $\delta n_B = 2n_0$ for our selected hadronic EOS with $m_0 = 600$ MeV and $n_L = 1.5n_0$.

For other choices of δn_B, we first exclude parameter combinations that cannot support NSs with masses

$\geq 2M_\odot$. Second, we apply radius constraints as illustrated in Fig. 3 to find whether there still exist parameter spaces in quark phase. Through this parameter space analysis, we determine the maximum allowable first-order transition strength δn_B and corresponding energy density discontinuity $\delta\varepsilon$ for our selected hadronic EOS. To satisfy all observational constraints within 1σ confidence level for our selected hadronic EOS, we find $\delta n_B \leq 1.12n_0$ with a corresponding energy density jump $\delta\varepsilon \leq 182$ MeV/fm^3. If we relax our criteria to require consistency with observations at the 2σ level, the constraints become $\delta n_B \leq 1.68n_0$ with $\delta\varepsilon \leq 273$ MeV/fm^3.

To complete our analysis, we extend our investigation to examine how the maximum allowable strength of first-order PTs varies with different matching densities n_L. Fig. 5 presents the results of this systematic study across the range $1.1n_0 \leq n_L \leq 2n_0$. The upper panel displays the maximum permitted density discontinuity δn_B as a function of the matching density, while the lower panel shows the corresponding maximum energy density jump $\delta\varepsilon$ versus n_L. In both panels, dashed curves represent constraints derived from requiring consistency with NS observations at the 1σ confidence level, while solid curves indicate the less stringent 2σ confidence level constraints. In Fig. 5, we find for a given density, the allowed PT strength decreases with increasing chiral invariant mass m_0. This behavior is expected since larger m_0 values lead to softer hadronic EOSs, making it more difficult to satisfy the $2M_\odot$ constraint when strong PTs are present. Also, at the lowest density ($n_B = 1.1n_0$), the allowed PT strength becomes nearly degenerate across different m_0 values. This convergence occurs because the EOS at low densities is primarily determined by saturation properties, which are used as input parameters for all m_0 values, resulting in similar low-density behavior regardless of the chiral invariant mass. Furthermore, for stiff hadronic EOSs (e.g., $m_0 = 600$ MeV) at higher densities ($n_L \gtrsim 1.9n_0$), the constraints from 1σ and 2σ confidence levels converge. This degeneracy arises because the corresponding M-R relations approach the observational limits from GW 170817 and PSR J0030+0451 (see Fig. 3), leaving less room for variation between different confidence levels.

3. SUMMARY AND DISCUSSION

In this work, we have systematically constrained the allowable strength of first-order PTs in the low-density region of NS matter using a unified theoretical framework that combines the PDM for hadronic matter, the NJL-type quark model for high-density matter, and a model-independent approach for the intermediate density region. Our analysis, incorporating observational constraints from NICER measurements and gravitational wave detections, establishes robust upper limits on the transition strength.

Our results provide insights into nucleon mass origin through the PDM framework. Inside the PDM, the nucleon mass is divided into into the chiral invariant component m_0 and the chiral symmetry breaking contribution m_σ. By systematically varying m_0 and constraining values consistent with NS observations, we probe different mass generation scenarios. Larger m_0 values lead to softer hadronic EOSs and more restrictive PT constraints, while smaller m_0 values allow stronger tran-
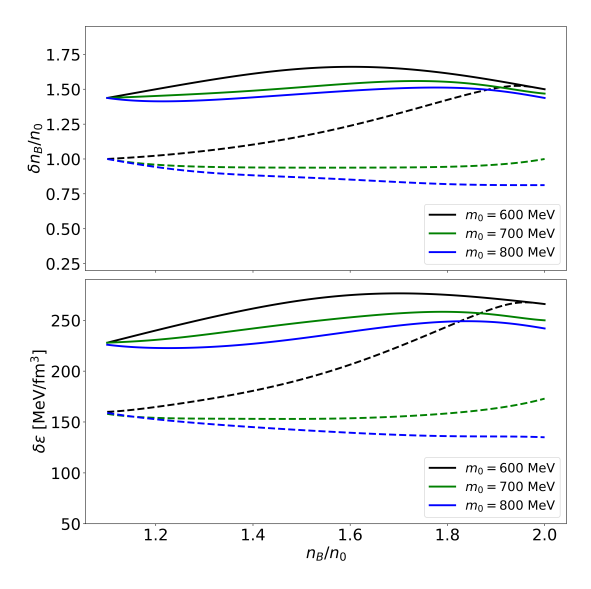

Figure 5. Maximum allowable strength of first-order PTs as a function of matching density. Upper panel: Maximum permitted baryon density discontinuity δn_B. Lower panel: Corresponding maximum energy density jump $\delta\varepsilon$. Dashed curves represent constraints derived from NS at 1σ confidence level, while solid curves show the less restrictive constraints at 2σ confidence level.

sitions. This demonstrates how astrophysical observations can inform fundamental QCD mechanisms underlying hadron mass generation.

Our results have profound implications for early deconfinement in NSs. The density regime $n_B \leq 2n_0$ encompasses where phase transitions to quark matter might occur well below typical deconfinement densities ($n_B \gtrsim 5n_0$). Previous studies in Ivanytskyi et al. (2023); Blaschke et al. (2023); Gärtlein et al. (2023) identified intersection points between hadronic and quark EOSs in similar density ranges below $2n_0$ and also proposed the possibility of the early deconfinement. Our approach provides a more general framework by employing a model-independent intermediate density EOS to quantify transition strengths consistent with current observations, avoiding simple extrapolations of either hadronic or quark models. The low-density nature of these transitions makes them accessible to terrestrial heavy-ion collision experiments at facilities such as FAIR and NICA, providing unique opportunities for cross-validation of theoretical predictions in density ranges overlapping with astrophysical conditions.

Our constraints also directly impact the detectability of PT signatures across multi-messenger channels. Gravitational waves from NS mergers carry distinctive PT imprints, while first-order transitions can liberate enormous energies ($\sim 10^{53}$ erg), potentially producing neutrino bursts and gamma-ray bursts. However, our

limits indicate that low-density transitions must be relatively weak to remain observationally consistent. These systematic constraints provide essential input for predicting signatures detectable by next-generation gravitational wave detectors.

Finally, we note that our analysis still depends on specific hadronic and quark EOS models and assumes quark matter relevance at $n_B \gtrsim 5n_0$. Earlier quark matter EOS onset would yield more stringent PT constraints. Future improvements in theoretical modeling and precise NS observations will refine our understanding of both phase transition dynamics and nucleon mass structure. In conclusion, our systematic analysis provides crucial guidance for understanding dense matter in NSs while offering insights into nucleon mass generation. These constraints will be essential for distinguishing theoretical scenarios of exotic matter phases and mass origin, contributing to our understanding of strongly interacting matter from microscopic to astrophysical scales.

APPENDIX

In this appendix, we construct neutron star matter EOS in both hadronic matter part and quark matter part.

A. HADRONIC MATTER EOS

We employ the parity doublet framework for hadronic EOS as discussed in ((Gao et al. 2022; Minamikawa et al. 2023)). In this approach, two types of nucleons with positive and negative parity states are treated as chiral partners, and their masses become degenerate when chiral symmetry is restored at high densities. This mass, known as the chiral invariant mass, is a key parameter in these models, significantly influencing the stiffness of the EOS. In particular, a larger m_0 results in weaker σ couplings to nucleons since the mass of nucleon is not completely derived from the σ fields. Correspondingly, the couplings to ω fields are reduced since at the nuclear saturation density n_0, the repulsive contributions of the ω fields must be counterbalanced by the attractive σ contributions. Beyond densities greater than n_0, the σ fields decrease while the ω fields increase, leading to an imbalance. As a consequence, a larger m_0 weakens the ω fields and softens EOS at supranuclear densities. Typical PDMs are σ-ω type mean field models, with some works also incorporating the isovector scalar meson $a_0(980)$, which is believed to appear in asymmetric matter, such as in neutron stars. However, as investigated in Ref. Kong et al. (2023), the inclusion of the $a_0(980)$ has a negligible impact on the properties of neutron stars, resulting in only a slight increase in the radius of less than 1km. In this study, we then consider the PDM model with $N_f = 2$ and include the vector meson mixing, such as the $\omega^2\rho^2$ interaction, as described in Ref. Gao et al. (2022).

The thermodynamic potential of the model in the mean-field approximation is calculated as

$$\begin{aligned}
\Omega_{\mathrm{PDM}} = {} & V_\sigma - V\left(f_\pi\right) \\
& + V_\omega + V_\rho + V_{\omega\rho} + \sum_{i=+,-}\sum_{x=p,n} \Omega_x \;,
\end{aligned} \tag{A1}$$

where $i = +, -$ denote the positive-parity ordinary nucleon $N(939)$ and negative-parity excited nucleon $N^*(1535)$. The mean-field potential $V(\sigma)$, V_ω, V_ρ and $V_{\omega\rho}$ are given by

$$\begin{aligned}
V(\sigma) &= -\frac{1}{2}\bar{\mu}^2\sigma^2 + \frac{1}{4}\lambda_4\sigma^4 - \frac{1}{6}\lambda_6\sigma^6 - m_\pi^2 f_\pi \sigma \;, \\
V_\omega &= -\frac{m_\omega^2}{2}\omega^2 \;, \\
V_\rho &= -\frac{m_\rho^2}{2}\rho^2 \\
V_{\omega\rho} &= -\lambda_{\omega\rho}(g_{\omega NN}\omega)^2(g_{\rho NN}\rho)^2 \;,
\end{aligned} \tag{A2}$$

with f_π the pion decay constant. Here, $\bar{\mu}, \lambda_4, \lambda_6$ and $\lambda_{\omega\rho}$ are parameters to be determined and the kinetic part of the thermodynamic potential Ω_x reads

$$\Omega_x = -2\int^{k_x^\pm}\frac{\mathrm{d}^3\mathbf{p}}{(2\pi)^3}\left(\mu_x^* - E_{\mathbf{p}}^i\right), \tag{A3}$$

with $E_{\mathbf{p}}^i = \sqrt{\mathbf{p}^2 + m_\pm^2}$ is the energy of relevant nucleon with mass $m_\pm$ and momentum $\mathbf{p}$, and $k_x^\pm = \sqrt{(\mu_x^*)^2 - m_\pm^2}$ is the fermi momentum for the relevant particle, in which μ_x^* is the effective chemical potential. We notice that we use the no-sea approximation, assuming that the structure of the Dirac sea remains the same for the vacuum and medium.

The masses of the positive- and negative-parity chiral partners are given by

$$m_\pm = \frac{1}{2}\left[\sqrt{\left(g_1 + g_2\right)^2\sigma^2 + 4\left(m_0\right)^2} \mp \left(g_1 - g_2\right)\sigma\right] \;, \tag{A4}$$

where $\pm$ sign denotes parity. The spontaneous chiral symmetry breaking yields the mass splitting between the two baryonic parity partners in each parity doublet. When the symmetry is restored, the masses in each parity doublet become degenerate: $m_\pm(\sigma = 0) = m_0$. The positive-parity nucleons are identified as the positively charged and neutral $N(939)$ states: proton (p) and neutron (n). Their negative-parity counterparts, denoted as p^* and n^*, are

identified as $N(1535)$ resonance. For a given chirally invariant mass, m_0, the parameters g_1 and g_2 are determined by the corresponding vacuum masses, $m_N = 939\text{MeV}, m_{N^*} = 1535\text{MeV}$. The effective chemical potentials for nucleons and their chiral partners are given by

$$
\begin{aligned}
\mu_p &= \mu_p^* = \mu_Q + \mu_B - g_{\omega NN}\omega - \frac{1}{2}g_{\rho NN}\rho \ , \\
\mu_n &= \mu_n^* = \mu_B - g_{\omega NN}\omega + \frac{1}{2}g_{\rho NN}\rho \ .
\end{aligned}
\tag{A5}
$$

The total thermodynamic potential of the hadronic matter in neutron stars is obtained by including the effects of leptons as

$$
\Omega_{\text{H}} = \Omega_{\text{PDM}} + \Omega_e,
\tag{A6}
$$

where Ω_e is the thermodynamic potentials for electrons given by

$$
\Omega_e = -2 \int^{k_F} \frac{\text{d}^3\mathbf{p}}{(2\pi)^3} \left(\mu_l - E_{\mathbf{p}}^l \right),
\tag{A7}
$$

Finally, we have the pressure in hadronic matter as

$$
P_{\text{H}} = -\Omega_{\text{H}}.
\tag{A8}
$$

Using the explicit parameter sets determined in Ref. Minamikawa et al. (2021), with fitting to the pion decay constant and hadron masses, as well as to the normal nuclear matter properties, we can calculate the corresponding EOS in the hadronic phase for different choices of the chiral invariant mass m_0.

B. QUARK MATTER EOS

Following Refs. Baym et al. (2018, 2019), we use the NJL quark model to describe the quark matter. The model includes three-flavors and $U(1)_A$ anomaly effects through the quark version of the KMT interaction. The coupling constants are chosen to be the Hatsuda-Kunihiro parameters which successfully reproduce the hadron phenomenology at low energy (Baym et al. (2018); Hatsuda & Kunihiro (1994)): $G\Lambda^2 = 1.835, K\Lambda^5 = 9.29$ with $\Lambda = 631.4\,\text{MeV}$, see the definition below. The couplings g_V and H characterize the strength of the vector repulsion and attractive diquark correlations whose range will be examined later when we discuss the NS constraints.

We can then write down the thermodynamic potential as

$$
\begin{aligned}
\Omega_{\text{CSC}} =\, &\Omega_s - \Omega_s \left[\sigma_f = \sigma_f^0, d_j = 0, \mu_q = 0 \right] \\
&+ \Omega_c - \Omega_c \left[\sigma_f = \sigma_f^0, d_j = 0 \right],
\end{aligned}
\tag{B9}
$$

where the subscript 0 is attached for the vacuum values, and

$$
\begin{aligned}
\Omega_s &= -2 \sum_{i=1}^{18} \int^{\Lambda} \frac{d^3\mathbf{p}}{(2\pi)^3} \frac{\epsilon_i}{2}, \\
\Omega_c &= \sum_i \left(2G\sigma_i^2 + Hd_i^2 \right) - 4K\sigma_u\sigma_d\sigma_s - g_V n_q^2,
\end{aligned}
\tag{B10}
$$

with σ_f are the chiral condensates, d_j are diquark condensates, and n_q is the quark density. In Eq.(B10), ϵ_i are energy eigenvalues obtained from inverse propagator in Nambu-Gorkov bases

$$
S^{-1}(k) = \begin{pmatrix} \gamma_\mu k^\mu - \hat{M} + \gamma^0\hat{\mu} & \gamma_5 \sum_i \Delta_i R_i \\ -\gamma_5 \sum_i \Delta_i^* R_i & \gamma_\mu k^\mu - \hat{M} - \gamma^0\hat{\mu} \end{pmatrix},
\tag{B11}
$$

where

$$
\begin{aligned}
M_i &= m_i - 4G\sigma_i + K\left|\epsilon_{ijk}\right|\sigma_j\sigma_k, \\
\Delta_i &= -2Hd_i, \\
\hat{\mu} &= \mu_q - 2g_V n_q + \mu_3\lambda_3 + \mu_8\lambda_8 + \mu_Q Q, \\
(R_1, R_2, R_3) &= (\tau_7\lambda_7, \tau_5\lambda_5, \tau_2\lambda_2).
\end{aligned}
\tag{B12}
$$

$S^{-1}(k)$ is 72×72 matrix in terms of the color, flavor, spin, and Nambu-Gorkov basis, which has 72 eigenvalues. $M_{u,d,s}$ are the constituent masses of u, d, s quarks and $\Delta_{1,2,3}$ are the gap energies. The $\mu_{3,8}$ are the color chemical potentials which will be tuned to achieve the color neutrality. The total thermodynamic potential including the effect of leptons is

$$\Omega_Q = \Omega_{\mathrm{CSC}} + \sum_{l=e,\mu} \Omega_l. \tag{B13}$$

The mean fields are determined from the gap equations,

$$0 = \frac{\partial \Omega_Q}{\partial \sigma_i} = \frac{\partial \Omega_Q}{\partial d_i}, \tag{B14}$$

From the conditions for electromagnetic charge neutrality and color charge neutrality, we have

$$n_j = -\frac{\partial \Omega_Q}{\partial \mu_j} = 0, \tag{B15}$$

where $j = 3, 8, Q$. The baryon number density n_B is determined as

$$n_q = -\frac{\partial \Omega_Q}{\partial \mu_q}, \tag{B16}$$

where μ_q is $1/3$ of the baryon number chemical potential. After determined all the values, we obtain the pressure as

$$P_Q = -\Omega_Q. \tag{B17}$$

REFERENCES

Abbott, B. P., et al. 2017a, Phys. Rev. Lett., 119, 161101, doi: 10.1103/PhysRevLett.119.161101

—. 2017b, Astrophys. J. Lett., 848, L12, doi: 10.3847/2041-8213/aa91c9

—. 2018, Phys. Rev. Lett., 121, 161101, doi: 10.1103/PhysRevLett.121.161101

Alford, M. G., & Sedrakian, A. 2017, Phys. Rev. Lett., 119, 161104, doi: 10.1103/PhysRevLett.119.161104

Baym, G., Furusawa, S., Hatsuda, T., Kojo, T., & Togashi, H. 2019, Astrophys. J., 885, 42, doi: 10.3847/1538-4357/ab441e

Baym, G., Hatsuda, T., Kojo, T., et al. 2018, Rept. Prog. Phys., 81, 056902, doi: 10.1088/1361-6633/aaae14

Benic, S., Blaschke, D., Alvarez-Castillo, D. E., Fischer, T., & Typel, S. 2015, Astron. Astrophys., 577, A40, doi: 10.1051/0004-6361/201425318

Blaschke, D., Shukla, U., Ivanytskyi, O., & Liebing, S. 2023, Phys. Rev. D, 107, 063034, doi: 10.1103/PhysRevD.107.063034

Bogdanov, S., Heinke, C. O., Özel, F., & Güver, T. 2016, Astrophys. J., 831, 184, doi: 10.3847/0004-637X/831/2/184

Busza, W., Rajagopal, K., & van der Schee, W. 2018, Ann. Rev. Nucl. Part. Sci., 68, 339, doi: 10.1146/annurev-nucl-101917-020852

Christian, J.-E., Schaffner-Bielich, J., & Rosswog, S. 2024, Phys. Rev. D, 109, 063035, doi: 10.1103/PhysRevD.109.063035

Detar, C. E., & Kunihiro, T. 1989, Phys. Rev. D, 39, 2805, doi: 10.1103/PhysRevD.39.2805

Dexheimer, V., Schramm, S., & Zschiesche, D. 2008, Phys. Rev. C, 77, 025803, doi: 10.1103/PhysRevC.77.025803

Fujimoto, Y., Fukushima, K., Hotokezaka, K., & Kyutoku, K. 2023, Phys. Rev. Lett., 130, 091404, doi: 10.1103/PhysRevLett.130.091404

Fujimoto, Y., Fukushima, K., & Murase, K. 2021, JHEP, 03, 273, doi: 10.1007/JHEP03(2021)273

Gao, B., & Harada, M. 2025, Phys. Rev. D, 111, 016024, doi: 10.1103/PhysRevD.111.016024

Gao, B., Minamikawa, T., Kojo, T., & Harada, M. 2022, Phys. Rev. C, 106, 065205, doi: 10.1103/PhysRevC.106.065205

Gao, B., Yan, Y., & Harada, M. 2024a, Phys. Rev. C, 109, 065807, doi: 10.1103/PhysRevC.109.065807

Gao, B., Yuan, W.-L., Harada, M., & Ma, Y.-L. 2024b, Phys. Rev. C, 110, 045802, doi: 10.1103/PhysRevC.110.045802

Gärtlein, C., Ivanytskyi, O., Sagun, V., & Blaschke, D. 2023, Phys. Rev. D, 108, 114028, doi: 10.1103/PhysRevD.108.114028

Gholami, H., Rather, I. A., Hofmann, M., Buballa, M., & Schaffner-Bielich, J. 2024. https://arxiv.org/abs/2411.04064

Guo, L.-J., Yang, W.-C., Ma, Y.-L., & Wu, Y.-L. 2025, Res. Astron. Astrophys., 25, 035017, doi: 10.1088/1674-4527/adbc37

Hatsuda, T., & Kunihiro, T. 1994, Phys. Rept., 247, 221, doi: 10.1016/0370-1573(94)90022-1

Huang, Y.-J., Baiotti, L., Kojo, T., et al. 2022, Phys. Rev. Lett., 129, 181101, doi: 10.1103/PhysRevLett.129.181101

Ivanytskyi, O., Blaschke, D., Fischer, T., & Bauswein, A. 2023, Acta Phys. Polon. Supp., 16, 1, doi: 10.5506/APhysPolBSupp.16.1-A104

Jido, D., Oka, M., & Hosaka, A. 2001, Prog. Theor. Phys., 106, 873, doi: 10.1143/PTP.106.873

Kojo, T., Baym, G., & Hatsuda, T. 2022, Astrophys. J., 934, 46, doi: 10.3847/1538-4357/ac7876

Komoltsev, O., & Kurkela, A. 2022, Phys. Rev. Lett., 128, 202701, doi: 10.1103/PhysRevLett.128.202701

Kong, Y. K., Minamikawa, T., & Harada, M. 2023, Phys. Rev. C, 108, 055206, doi: 10.1103/PhysRevC.108.055206

Lenzi, C. H., & Lugones, G. 2012, Astrophys. J., 759, 57, doi: 10.1088/0004-637X/759/1/57

Li, B.-A., Cai, B.-J., Xie, W.-J., & Zhang, N.-B. 2021, Universe, 7, 182, doi: 10.3390/universe7060182

Marczenko, M., Blaschke, D., Redlich, K., & Sasaki, C. 2020, Astron. Astrophys., 643, A82, doi: 10.1051/0004-6361/202038211

Marczenko, M., Redlich, K., & Sasaki, C. 2022, Phys. Rev. D, 105, 103009, doi: 10.1103/PhysRevD.105.103009

Miller, M. C., et al. 2019, Astrophys. J. Lett., 887, L24, doi: 10.3847/2041-8213/ab50c5

—. 2021, Astrophys. J. Lett., 918, L28, doi: 10.3847/2041-8213/ac089b

Minamikawa, T., Gao, B., Kojo, T., & Harada, M. 2023, Symmetry, 15, 745, doi: 10.3390/sym15030745

Minamikawa, T., Kojo, T., & Harada, M. 2021, Phys. Rev. C, 103, 045205, doi: 10.1103/PhysRevC.103.045205

Most, E. R., Weih, L. R., Rezzolla, L., & Schaffner-Bielich, J. 2018, Phys. Rev. Lett., 120, 261103, doi: 10.1103/PhysRevLett.120.261103

Motohiro, Y., Kim, Y., & Harada, M. 2015, Phys. Rev. C, 92, 025201, doi: 10.1103/PhysRevC.92.025201

Ozel, F., Psaltis, D., Guver, T., et al. 2016, Astrophys. J., 820, 28, doi: 10.3847/0004-637X/820/1/28

Raaijmakers, G., Greif, S. K., Hebeler, K., et al. 2021, Astrophys. J. Lett., 918, L29, doi: 10.3847/2041-8213/ac089a

Sasaki, C., & Mishustin, I. 2010, Phys. Rev. C, 82, 035204, doi: 10.1103/PhysRevC.82.035204

Weinberg, S. 1969, Phys. Rev., 177, 2604, doi: 10.1103/PhysRev.177.2604

Yuan, W.-L., Gao, B., Yan, Y., & Xu, R. 2025. https://arxiv.org/abs/2502.17859

Yuan, W.-L., & Li, A. 2024, Astrophys. J., 966, 3, doi: 10.3847/1538-4357/ad354f

Zschiesche, D., Tolos, L., Schaffner-Bielich, J., & Pisarski, R. D. 2007, Phys. Rev. C, 75, 055202, doi: 10.1103/PhysRevC.75.055202